# A Generalized Model for Two-Element Biomimetic Antenna Arrays

Patrik Grüner, *Student Member, IEEE,* Tobias Chaloun, *Member, IEEE,*
and Christian Waldschmidt, *Senior Member, IEEE*

***Abstract*—Biomimetic Antenna Arrays (BMAAs) are antenna systems enabling an improved angle estimation for small apertures by mimicking the hearing system of the fly *Ormia ochracea*. This is achieved by a special kind of coupling applied to the antenna elements inspired by the insect. However, recent designs of BMAAs rely on a strong mutual coupling between the antenna elements. In this paper, it will be shown that the strong mutual coupling is not needed for a BMAA at the antenna side, and a generalized model of the biomimetic antenna system is theoretically derived, evaluated, and verified by measurements. This new model also gives an intuitive insight into the working principle of the biomimetic antenna system.**

***Index Terms*—Biomimetic antenna arrays, antenna arrays, biologically-inspired antennas, direction-of-arrival (DoA) estimation**

## I. Introduction

ANGLE estimation using antenna arrays is usually done by evaluating the phase progression between the individual antenna elements. Therefore, the antenna element separation is usually chosen as large as possible to maximize this phase progression without getting ambiguity. However, accurate angle estimation is a challenge when only a small aperture is available because of space constraints due to costs or large wavelengths. Several methods were introduced overcoming this issue [1], [2], [3].

Looking in the nature, the parasitic fly *Ormia ochracea* is facing a similar challenge. With an ear separation of 1 mm only it needs to localize a cricket to deposit its eggs. The cricket is identified by its mating call at 5 kHz, i. e., the ears of *Ormia ochracea* are separated by $\lambda/70$ in terms of the wavelength $\lambda$ of interest. According to common theory the angle estimation performance should be quite poor but *Ormia ochracea* achieves an angle estimation accuracy of $2^\circ$ with the help of specially coupled ears [4].

The hearing system of the fly was thoroughly analyzed in [5] and a mechanical model was set up representing the dominant dynamical properties of the ears of *Ormia ochracea*. The purpose of this coupling is to mechanically increase the delay (phase) of an incoming signal between the ears. As a consequence, the angle of arrival can be distinguished more accurately. This model, which is briefly reviewed in Section II, was used to build up microphones which allow a remarkable increase in angular separability and therefore are used, e. g., in hearing aids [6], [7].

As a next step, the mechanical model was converted to an electrical model by the well-known analogy between mechanical and electrical systems and was then used to build up an antenna system with similar characteristics as the fly's auditory system [8], [9], [10]. This model was later extended by considering the strong mutual coupling of electrically small antenna arrays [11], [12]. For this electrical model a design process was proposed. Also, a fundamental trade-off of the biomimetic antenna system was revealed: Each increase in phase difference comes at the cost of output power. This means that increasing the ability of measuring the incoming angle is decreasing the maximal range of the underlying system. The findings were verified by a BMAA consisting of two dipole antennas at 600 MHz. The external coupling network representing the hearing system of the animal was built up using lumped elements.

Inspired by the electrical model and the design process, several BMAA designs were presented using planar antennas at 400 MHz [13], [14] and 20 GHz [15] where also a coupling network in planar microstrip technology using distributed elements was implemented. An extension of the BMAA concept to three radiating elements was shown in [16], [17]. An indoor tracking system using BMAAs at a frequency of 20 MHz was presented in [18].

The current research shows that BMAAs are narrow-band systems. Several works were conducted to conquer this issue by using non-Foster matching networks [19] or electrically tunable coupling networks [20].

According to some publications the radiation pattern of an antenna array becomes narrower when using biomimetic coupling [13], [14], [21]. Simulation results show a significant reduction in the beamwidth depending on the choice of the coupling network elements for antenna elements spaced $\lambda/10$ apart at frequencies of 400 MHz and 1 GHz.

The angle estimation capability of BMAAs were first analyzed by Akcakaya et al. They solved the differential equations of the mechanical model and analyzed the angle estimation accuracy by computing the Cramer-Rao-Bound (CRB) [22]. Later, the solutions of the differential equations of the mechanical model were transformed to radio frequencies, and the biomimetic coupling was regarded as a multiple-input multiple-output filter at the antenna array outputs [23]. With this model, which was set-up for 10 antenna elements, also the

This work was funded by the German Research Foundation (DFG, Deutsche Forschungsgemeinschaft) under Grant WA 3506/6-1. *(Corresponding author: Patrik Grüner.)*

The authors are with the Institute of Microwave Engineering, Ulm University, 89081 Ulm, Germany (e-mail: patrik.gruener@uni-ulm.de)

Color versions of one or more of the figures in this paper are available online at https://ieeexplore.ieee.org.

Digital Object Indentifier 10.1109/TAP.2018.2888829

CRB was calculated showing a significant increase in angle estimation capability compared to an antenna array with the same spacings and without biomimetic coupling. However, these publications focused on analytical investigations as well as numerical simulations. In [24] radar measurements were performed with biomimetic antenna arrays and compared to conventional antenna arrays with the same antenna element spacing. Here, an increase in angle estimation accuracy of factor 2 was achieved. In [25], the boundaries of the fundamental trade-off of the BMAA was investigated and an upper limit of the angular resolution enhancement without sacrificing power was derived.

However, the current electrical model of the BMAA relies on a strong mutual coupling of the antenna elements. While mutual antenna coupling has drawbacks for the antenna performance, this also limits the choice of usable antenna elements and works only for antenna arrays with very small element separation. Starting from the mechanical model, this work introduces a generalized model which allows to separate the biomimetic coupling from the mutual antenna coupling and also illustrates the working principle of the biomimetic antenna array in an intuitive way. By applying this generalized model basically every antenna element can be used for a BMAA independent of the size of the antenna or the separation of the array elements. The model extends the BMAA theory in a way that it is not limited anymore to electrically small antenna arrays but can also enhance the angle estimation for larger arrays.

Section II compares BMAA models introduced so far, shows their limitations and proposes a generalized electrical model. This model is then analytically evaluated in Section III and a design process is given in Section IV. The different electrical models are then compared in Section V. Section VI finally proves the theoretical investigations with measurements of a fabricated prototype.

## II. BMAA Models

In this section, the recent models of the BMAA are discussed. It will be shown, that current electrical models do not fully match with the mechanical model. At the end of the section, a generalized electrical model is introduced fixing the shortcomings of today's electrical models.

### A. Mechanical Model

All derivations concerning the BMAA so far are based on the mechanical model of the fly *Ormia ochracea*'s hearing system shown in Fig. 1. It consists of two rigid bars each mounted on a solid pivot point. The other side of the bar is connected to the ground by a combination of a spring and a damper. This combination models the fly's ears with their dynamical properties. The two bars are also connected by a spring/damper combination ($k_3$ and $c_3$) modeling the coupling of the two ears. The forces $F_1$ and $F_2$ originating from the incoming sound wave mark the inputs of the system whereas the displacements $y_1$ and $y_2$ at the outer ends of the bars are the outputs. The values for $F$ are modeled to have equal amplitudes but differ in phase according to the angle of incidence $\theta$ of the sound wave. This model was derived and thoroughly analyzed in [5]. In particular, the lumped element values were determined so that the mechanical model resembles the behavior of the fly's hearing system very closely. The validity of the mechanical model was verified by measurements.

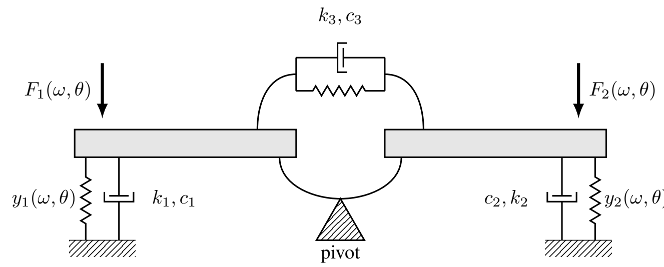


Fig. 1. Mechanical model of the hearing system of the fly *Ormia ochracea* [5].

To explain the working principle of the system, the extreme cases "no coupling" and "infinite coupling" are considered. If no coupling is present between the bars ($k_3 \to 0$, $c_3 \to 0$), the ears are completely independent from each other and the output value $y_{1/2}$ depends only on the respective input values $F_{1/2}$. The amplitudes of $y_{1/2}$ are equal and the phases only depend on the physical aperture size.

In the case of an infinitely strong coupling between the ears of the fly ($k_3 \to \infty$, $c_3 \to \infty$), the two rigid bars in the model now effectively become one solid bar. This bar is still mounted on the triangular pivot point and can tip around it. If a plane wave is now vertically incident on the model (i. e., $\theta=0$) the bar is loaded equally on both sides by the forces $F_1$ and $F_2$, because $F_1$ and $F_2$ are now equal both in amplitude and in phase (common mode excitation). Because of the mount at the pivot point the bar will not move, i. e., the output values $y_{1/2}$ are zero. When the plane wave is incident from an angle $\theta \neq 0$ (i. e., $|F_1|=|F_2|$, $\arg F_1 = -\arg F_2$, differential mode excitation), this leads to a displacement of the bar: It is tipping towards one direction. In this case the amplitudes of the output values $y_{1/2}$ are always equal (due to the rigid bar) and $180^\circ$ out of phase.

The real behavior of the model is a superposition of these two extreme cases.

### B. Electrical Model

In [9] the mechanical model was converted to an electrical model. The conversion was demonstrated in two ways: One method used the analogy of mechanical force and electrical current, and the other used the analogy between mechanical force and electrical voltage. Both methods lead to different equivalent circuits which are shown in detail in [9]. In this article only the first method is considered for the sake of simplicity, but the investigations are also valid for the second one. The equivalent circuit derived in [9] is depicted in Fig. 2(a). Each of the two antennas is modeled by an ideal current source. The amplitudes of the current sources are equal and the phases differ in the sign. The phase difference between the currents follows $kd\sin\theta$ with $k=2\pi/\lambda$ the free-space wave

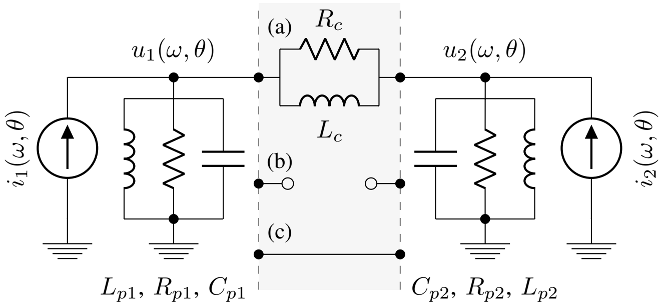


Fig. 2. Electrical model of the BMAA according to [9], [12] with (a) biomimetic coupling, (b) no coupling, and (c) infinitely high coupling.

number, $\lambda$ the wavelength, $d$ the separation of the antennas, and $\theta$ the incident angle of the plane wave. The capacitors $C_{p1}$ and $C_{p2}$ are the equivalents for the bars in the mechanical model, the elements $L_{p1}$, $L_{p2}$, $R_{p1}$, and $R_{p2}$ match with the springs and the dampers $k_1$, $k_2$, $c_1$, and $c_2$ in the mechanical model. At the same time, $R_c$ and $L_c$ are the equivalents of the coupling elements $k_3$ and $c_3$. The output values of the system are the voltages $u_1$ and $u_2$. The mutual coupling of the antenna elements, like it is introduced in later publications [11], [12], is not yet considered.

For this model, the same evaluations concerning the extreme cases shall be performed to investigate the complete equivalence between mechanical and electrical model. At first, the uncoupled case is investigated, i. e., the elements $R_c$ and $L_c$ are substituted by an open, cf. Fig. 2(b). The antennas are completely independent from each other and the output voltages $u_1$ and $u_2$ depend only on the input currents $i_1$ and $i_2$ as well as the lumped element values. The phase difference between input and output values, respectively, is thereby equal and only dependent on the physical aperture size, i. e., the separation $d$ of the antennas. This behavior is consistent with the mechanical model.

Fig. 2(c) shows the case of an infinitely strong coupling between the antennas. The elements $R_c$ and $L_c$ are replaced by a short circuit. Again, the excitation with common and differential mode is considered. In the case of the common mode excitation, the exciting currents $i_1$ and $i_2$ are identical in amplitude and phase. This leads to voltages $u_1$ and $u_2$ across the elements $R_{p1/2}$ and $C_{p1/2}$ which are also equal in amplitude and phase. As a consequence, there is no potential difference between the two antennas and no current is flowing through the short circuited connection. But the voltages $u_1$ and $u_2$ are not zero. This is in contrast to the mechanical model whose equivalent quantity $v{=}\dot{y}$ has to be zero in this case because the solid bar cannot move. In the case of the differential mode excitation, the exciting currents $i_1$ and $i_2$ are still equal in amplitude but now differ in phase ($|i_1|{=}|i_2|$, $\arg i_1{=}-\arg i_2$). The currents lead to voltages $u_1$ and $u_2$ across the elements $L_{p1/2}$, $R_{p1/2}$, and $C_{p1/2}$, which cannot be equal due to the differing excitation. However, the voltages have to be the same. At the same time, the equivalence to the mechanical model demands a phase difference of 180° between $u_1$ and $u_2$ which also cannot be realized with this model. For this reason, the electrical model has to be modified.

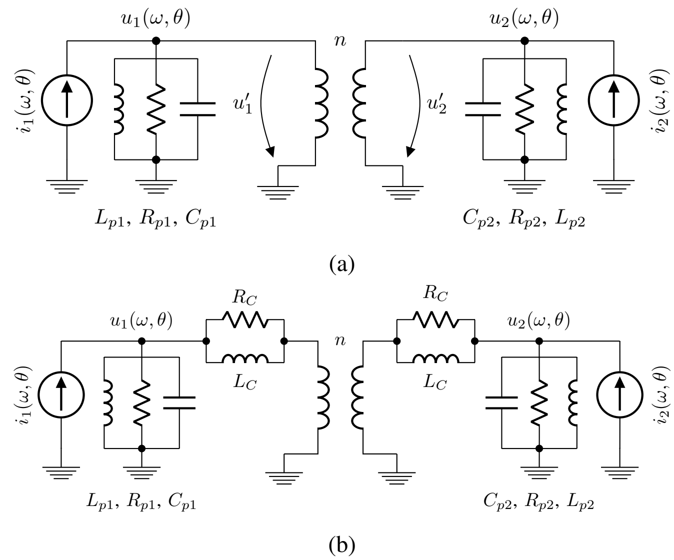


Fig. 3. Generalized electrical model of the BMAA with (a) infinitely strong coupling and (b) biomimetic coupling.

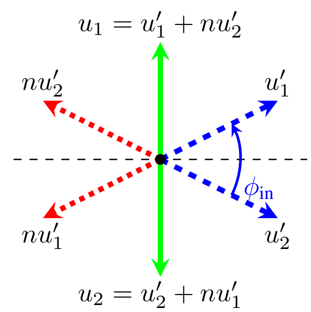


Fig. 4. Vector plot for the generalized model with infinite coupling. The dashed blue vectors show the input of the system, the solid green vectors the output.

### C. Generalized Electrical Model

Comparing the mechanical model in Fig. 1 and the electrical model in Fig. 2(a) it can be noticed that the pivot point in the mechanical model around which the bars are tipping, has no equivalence in the electrical model. Because of the fundamental impact on the working principle of the hearing system of *Ormia ochracea*, this element has to be properly considered in the electrical model.

For the synthesis of the new model the case of infinite coupling is considered first. The rigid bar in the mechanical model (cf. Fig. 1) which is mounted on the pivot element is in this case a lever bar with two equally long levers. They can be modeled in the electrical domain with a transformer. The antennas are still modeled by an RLC combination, cf. Fig. 3(a). In the model described in Section II-B the output voltages $u_1$ and $u_2$ do not vanish for a vertically incident plane wave, as it is predicted from the mechanical model. In the new model this is the case if the turning ratio $n$ of the transformer is chosen to $n{=}-1$. The voltage $u'_1$ generated on the left side by the current source $i_1$ over the left RLC combination is transferred over the transformer resulting in a voltage with negative sign on the right side. The same is

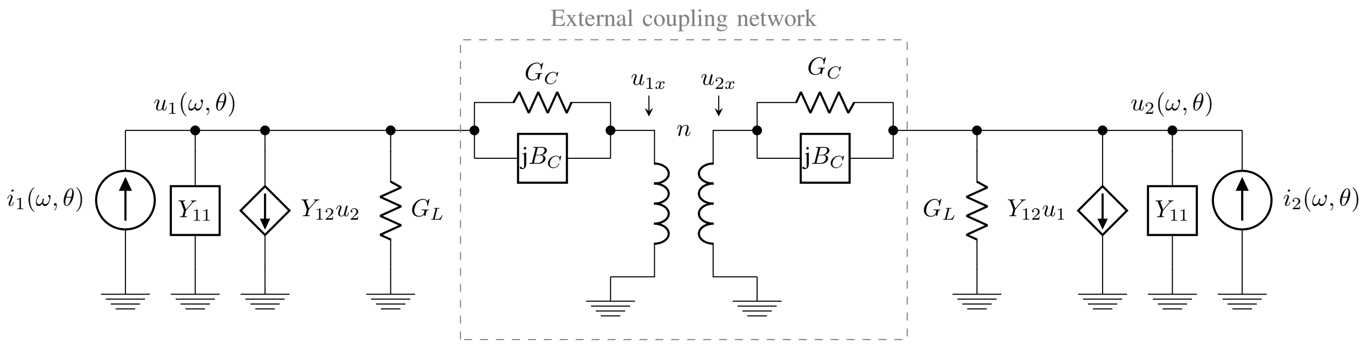


Fig. 5. Generalized electrical model of the two-element BMAA with an external coupling network. Mutual antenna coupling is considered by the voltage controlled current sources (cf. [12]).

true for the voltage $u_2'$ on the right side. As a result, the two voltages $u_1'$ and $n\,u_2'$ as well as $u_2'$ and $n\,u_1'$ cancel out so that for a vertically incident wave ($\theta{=}0$) both output voltages are zero: $u_1{=}u_2{=}0$.

For an inclined incident wave ($\theta{\neq}0$) the situation can be illustrated by means of a vector plot, see Fig. 4. Both voltages $u_1'$ and $u_2'$ are depicted here as vectors with equal amplitudes (dashed blue). The phase angle between the two vectors is $\phi_{\text{in}}{=}kd\sin\theta$. Additionally, the voltages after the transformation over the transformer are plotted (dotted red). They still have the same amplitude but are shifted in phase by $180°$ due to the turning ratio of $n{=}{-}1$. The sum of direct (dashed blue) and transformed voltage (dotted red) give the real voltages $u_1$ and $u_2$ which can be measured (solid green). The phase angle between these two voltages now is always $180°$, independent on the incidence angle of the wave. Only the amplitude of the resulting vector changes with the incidence angle $\theta$. This is fully consistent with the mechanical model.

For a complete equivalence between the mechanical and the electrical model the coupling elements which are modeled by the spring $k_3$ and the damper $c_3$ in Fig. 1 are still missing in the electrical model. The principle function of these elements is the scaling of the amplitude of the transformed signal (damper) and the scaling of the coupling phase (spring). In the electrical model, this behavior is modeled by the parallel connection of an inductor $L_C$ and a resistor $R_C$, cf. Fig. 3(b). For the basic functionality of the system this combination of inductor and resistor is needed only on one side of the transformer. As a matter of symmetry and especially for the practical realization later on, these elements are placed on both sides of the transformer.

## III. Analytical Description

In this section the new generalized electrical model will be described analytically. The derivations follow the conventions introduced in [11], [12]. As in [12], the Y-parameter representation of the antennas will be used instead of the RLC representation. Additionally, the mutual antenna coupling is considered. To couple out the voltages, the antenna is loaded by the conductance $G_L$. The inductance $L_C$ is generalized to the susceptance $B_C$ to be either an inductor or a capacitor. The modified circuit is depicted in Fig. 5. The input values of the system are the currents $i_1$ and $i_2$, the respective output values are the voltages $u_1$ and $u_2$. The excitation is modeled as in [11], [12] by

$$i_1(\theta) = A_0\,\mathrm{e}^{-\mathrm{j}\alpha}\,, \tag{1}$$
$$i_2(\theta) = A_0\,\mathrm{e}^{\mathrm{j}\alpha}\,, \tag{2}$$

with an amplitude $A_0$ and $\alpha{=}kd\sin(\theta)/2$ to model the angle dependent phase progression proportional to the physical aperture size $d$.

For the calculation of the output voltages $u_1$ and $u_2$ the common and differential mode of the system will be evaluated separately. For the common mode excitation it holds

$$i_{1,c}(\theta) = A_0\,\cos\alpha\,, \tag{3}$$
$$i_{2,c}(\theta) = A_0\,\cos\alpha\;. \tag{4}$$

This excitation leads to two equal voltages on both sides of the transformer. Due to the turning ratio of $n{=}{-}1$, the voltages with the same absolute value are added with negative sign and therefore, a virtual ground is created at the transformer for all incident angles $\theta$, i. e., $u_{1x}(\theta){=}u_{2x}(\theta){=}0$. Thus, the common mode voltage can be calculated by the parallel connection of all elements according to

$$u_{1,c}(\theta) = \frac{i_{1,c}(\theta)}{Y_{11}+Y_{12}+G_L+G_C+\mathrm{j}B_C} = u_{2,c}(\theta)\;. \tag{5}$$

Note that the common mode voltage is directly dependent on the coupling element values. Additionally, the common mode voltages are equal on both sides of the transformer.

The next step is the differential mode excitation for which the input values are modeled as follows:

$$i_{1,d}(\theta) = -\mathrm{j}A_0\,\sin\alpha\,, \tag{6}$$
$$i_{2,d}(\theta) = \mathrm{j}A_0\,\sin\alpha\;. \tag{7}$$

This excitation results in two currents at both sides of the transformer. While the current from source 2 is flowing into the transformer, the current from current source 1 is flowing out of the transformer. After transformation with a turning ratio $n{=}{-}1$, the transformed and the source current on each side cancel each other due to their opposite sign. As a consequence, no current is flowing through the coupling elements $G_C$ and $B_C$, and thus there is no voltage drop. The transformer acts like an open in this case, i.e., $u_{1x}(\theta){=}u_1(\theta)$

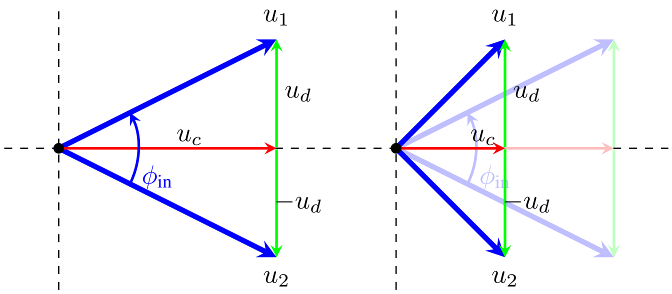


(a) (b)

Fig. 6. Vector plots for the generalized BMAA model (a) without and (b) with the biomimetic coupling (mutual coupling of antenna elements not yet considered).

and $u_{2x}(\theta)=u_2(\theta)$ for all $\theta$. The differential voltage $u_{1,d}(\theta)$ can now be calculated by the parallel connection of the remaining elements:

$$u_{1,d}(\theta) = \frac{i_{1,d}(\theta)}{Y_{11} - Y_{12} + G_L} = -u_{2,d}(\theta)\ . \tag{8}$$

Note that this equation is independent from the values of the coupling network. The differential voltages of the right and left side differ by the factor $-1$.

The voltages $u_1$ and $u_2$ are then given by the superposition of common and differential voltages:

$$u_1(\theta) = u_{1,c}(\theta) + u_{1,d}(\theta)\,, \tag{9}$$
$$u_2(\theta) = u_{2,c}(\theta) + u_{2,d}(\theta)\,. \tag{10}$$

For the explanation of the working principle of the biomimetic coupling, the vector plot is considered again. The output voltages $u_1$ and $u_2$ according to (9) and (10) are displayed in Fig. 6(a). They consist of the common mode voltage $u_c$ which is the same for both output voltages and the differential mode voltage $u_d$ having opposite signs depending on the respective output voltage. The phase angle $\phi_{\text{in}}$ only depends on the physical aperture size $d$. By varying the coupling network elements $B_C$ and $G_C$, the common mode voltage $u_c$ can now be scaled. At the same time, the differential mode voltage $u_d$ is not altered in any way because it is independent of the coupling network parameters. Fig. 6(b) shows the vector plot for this case with an exemplary set of parameters. In the same extent as $u_c$ is decreased, the phase angle $\phi_{\text{out}}$ between the voltages $u_1$ and $u_2$ is increased. Due to this effect, the amplitudes of the voltage vectors are also decreased. This is the well-known trade-off of the biomimetic antenna system to get enhanced phase sensitivity at the expense of output power [11], [15]. In the extreme case of infinite coupling ($G_C \to \infty$, $B_C \to \infty$), the common mode voltage is completely suppressed and both differential voltages with amplitude $u_d$ and opposite signs remain (cf. Fig. 3(a)).

A signal flow chart summarizing the working principle of the biomimetic antenna array is shown in Fig. 7. The factor $A$ depends on the antenna parameters as well as the coupling network parameters whereas the factor $B$ depends only on the antenna parameters.

In contrast to [12], the generalized electrical model exhibits a significantly easier relationship between the coupling network and the phase progression because only the common mode voltage and not the differential mode voltage is influenced by the coupling network parameters.

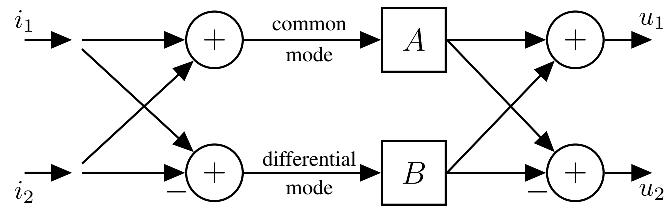


Fig. 7. Signal flow chart of the generalized model using an uncoupled antenna array ($Y_{12}$=0) with input currents $i_1$ and $i_2$ and output voltages $u_1$ and $u_2$. The factor $A$ is dependent on the coupling network parameters $G_C$ and $B_C$ while the factor $B$ is not.

## IV. Design Process

Two parameters were introduced so far to describe the BMAA on system level: the phase gain $\eta$ and the normalized output power $L_{\text{out}}$ [12], [15]. Both compare the BMAA to a regular antenna with the same antenna elements with the same spacing but without the coupling network. The phase gain is defined in boresight direction by dividing the slopes of the phase progression curves at the terminals of the BMAA ($\phi_{\text{out}}$) and the regular antenna array ($\phi_{\text{in}}$):

$$\eta = \frac{\left.\frac{\mathrm{d}\phi_{\text{out}}}{\mathrm{d}\theta}\right|_{\theta=0}}{\left.\frac{\mathrm{d}\phi_{\text{in}}}{\mathrm{d}\theta}\right|_{\theta=0}}\ . \tag{11}$$

It basically describes the increase in steepness of the BMAA phase difference curve compared to the regular antenna phase difference curve. The reduction of the output power level is quantified by the dimensionless quantity $L_{\text{out}}$:

$$L_{\text{out}} = \frac{P_{\text{out,BMAA}}}{P_{\text{out,reg. Array}}}\ . \tag{12}$$

This value is always less than or equal to 1. Fig. 8 shows a typical phase difference curve and output power level of a BMAA with a phase gain of $\eta$=5 and $L_{\text{out}}=-10\,\text{dB}$.

In this section it is derived how to set up the coupling network parameters for the generalized model to achieve a desired phase gain $\eta$. The antenna parameters $Y_{11}=G_{11}+\mathrm{j}B_{11}$ and $Y_{12}=G_{12}+\mathrm{j}B_{12}$ are assumed to be known and the unknown element values $G_C$ and $B_C$ are calculated. The conductance $G_L$ is kept constant (e. g., 20 mS).

The starting point of the design process is, similar as described in [12], the equation

$$\frac{u_2}{u_1} = \frac{1 + \mathrm{j}\frac{Y_{11}+Y_{12}+G_L+G_C+\mathrm{j}B_C}{Y_{11}-Y_{12}+G_L}\tan\alpha}{1 - \mathrm{j}\frac{Y_{11}+Y_{12}+G_L+G_C+\mathrm{j}B_C}{Y_{11}-Y_{12}+G_L}\tan\alpha} = \frac{1+\mathrm{j}z\tan\alpha}{1-\mathrm{j}z\tan\alpha}\,, \tag{13}$$

where the following abbreviation for the complex number $z$ was introduced:

$$z = \frac{G + G_{12} + G_C + \mathrm{j}b}{G - G_{12} + \mathrm{j}a}\ . \tag{14}$$

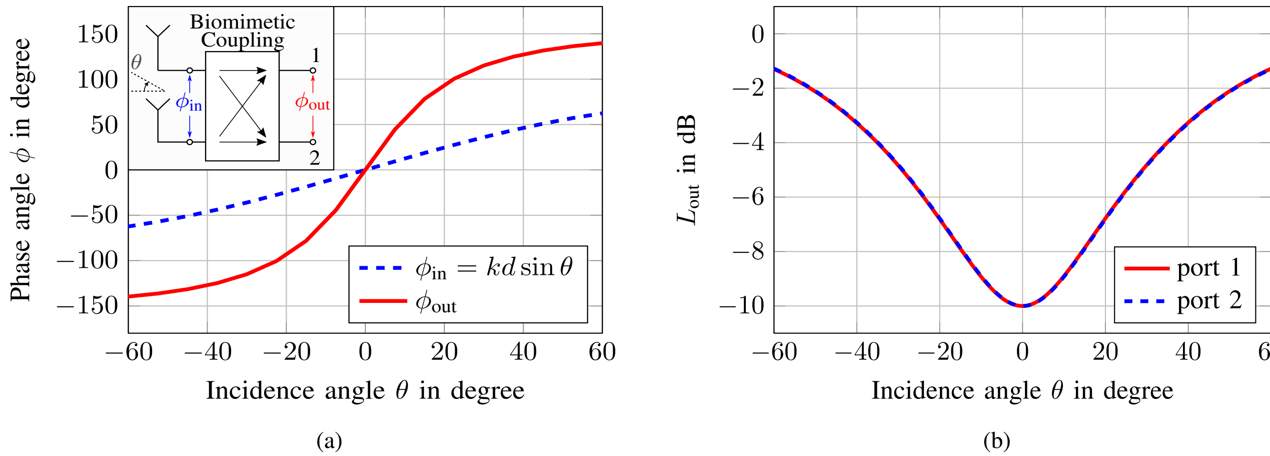


Fig. 8. Typical phase difference curves (a) and output power level $L_{\text{out}}$ (b) for a biomimetic antenna array with phase gain $\eta = 5$ and $L_{\text{out}} = -10\,\text{dB}$. The two curves for $L_{\text{out}}$ are identical and lie on top of each other.

The variables $b$, $a$, and $G$ are defined as follows:

$$b := B_{11} + B_{12} + B_C \,, \tag{15}$$
$$a := B_{11} - B_{12} \,, \tag{16}$$
$$G := G_{11} + G_L \,. \tag{17}$$

Equation (14) can be split into a real and an imaginary part [11] leading to

$$z = \frac{G^2 - G_{12}^2 + G_C(G - G_{12}) + ab}{(G - G_{12})^2 + a^2} + \mathrm{j}\,\frac{b(G - G_{12}) - a(G + G_{12} + G_C)}{(G - G_{12})^2 + a^2} \tag{18}$$
$$= \eta + \mathrm{j}\xi \,, \tag{19}$$

where $\eta$ is the realized phase gain in boresight direction according to (11). The normalized output power level $L_{\text{out}}$ is calculated from the circuit model in Fig. 5. This model can be used for the BMAA as well as for the conventional antenna array by neglecting the elements of the biomimetic coupling network (dashed box). The Y-parameters for both antenna arrays are the same because of the very same radiating elements. To get a fair comparison on how the two antenna arrays behave on a given system, the load conductances $G_L$ are also chosen equal. Considering only the boresight region (i.e., $u_d \approx 0$), the normalized output power level can be calculated as follows (cf. (12)):

$$L_{\text{out}} = \frac{|u_{c,\text{BMAA}}|^2}{|u_{c,\text{conv}}|^2} = \frac{|Y_{11} + Y_{12} + G_L|^2}{|Y_{11} + Y_{12} + G_L + G_C + \mathrm{j}B_C|^2} . \tag{20}$$

Since both antenna arrays have different impedances but the same loads, mismatch losses can occur. These losses are already included in (20).

In the design process, the maximum phase gain shall be at $\theta$=0, therefore, the parameter $\xi$ is set to zero [26]:

$$\xi = \frac{b(G - G_{12}) - a(G + G_{12} + G_C)}{(G - G_{12})^2 + a^2} \overset{!}{=} 0 \,. \tag{21}$$

Rearranging this equation leads to the correspondence

$$b = a\left(\frac{G + G_{12} + G_C}{G - G_{12}}\right) . \tag{22}$$

Inserting (22) into the expression for $\eta$ in (18) leads to

$$\eta = \frac{(G + G_{12}) + G_C + a^2\left(\frac{G + G_{12} + G_C}{(G - G_{12})^2}\right)}{(G - G_{12}) + a^2 \frac{1}{G - G_{12}}} . \tag{23}$$

In case of no mutual antenna coupling is present ($G_{12}$=0), (23) simplifies to

$$\eta = \frac{G^3 + G^2 G_C + a^2(G + G_C)}{G^3 + Ga^2} . \tag{24}$$

Apparently, besides the antenna parameters and the load conductance $G_L$, the conductance $G_C$ is a key parameter for the phase gain synthesis. In case of $G_C$=0 (open) no phase gain can be realized, i. e., $\eta$=1.

Equation (23) depends only on the given antenna parameters and the conductance $G_C$. This can be used to derive a formula for $G_C$ as a function of the desired phase gain $\eta$. From (23) follows by rearranging

$$G_C = \eta(G - G_{12}) - (G + G_{12}) \,. \tag{25}$$

If now the parameter $G_C$ is known, the coupling susceptance $B_C$ can be determined using (22):

$$B_C = a\left(\frac{G + G_{12} + G_C}{G - G_{12}}\right) - B_{11} - B_{12} \,, \tag{26}$$
$$= \eta(B_{11} - B_{12}) - (B_{11} + B_{12}) \,. \tag{27}$$

Depending on the sign of $B_C$ it can be realized as an inductor ($B_C < 0$) or as a capacitor ($B_C > 0$).

If no mutual antenna coupling is present ($G_{12}$=$B_{12}$=0), (25) and (27) simplify to

$$G_C|_{Y_{12}=0} = G(\eta - 1) \,, \tag{28}$$
$$B_C|_{Y_{12}=0} = B_{11}(\eta - 1) \,. \tag{29}$$

## V. Discussion of the Different Models

This section links the generalized model proposed in the previous sections to the electrical model in [12]. For that purpose, some important equations of [12] are summarized in Appendix A. It will be shown that this model is still valid as long as a strong mutual coupling between the antenna elements

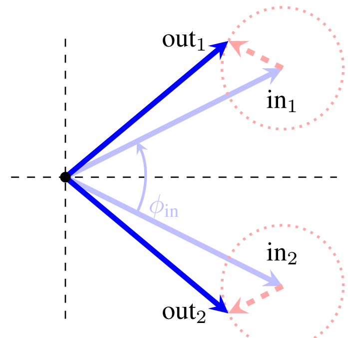


Fig. 9. Vector plot for the BMAA model with mutual antenna coupling (dashed red). An exemplary coupling with a magnitude of 0.25 and a phase of 180° has been considered.

is considered. To differentiate between the two models, all parameters relating to the model of [12] are marked with a bar (e. g., $\bar{\eta}$).

Comparing (13) with the respective equation in [12] (cf. (40)) it can be noticed, that the equations are the very same but with different expressions for $z$. When comparing $\bar{z}$ from [12] (cf. (41)) with $z$ in (14) and neglecting the mutual antenna coupling ($G_{12}$=$B_{12}$=0) the following relations result:

$$2\bar{G}_{12} = G_C\,, \tag{30}$$
$$2\bar{B}_{12} - \bar{B}_2 = B_C\,. \tag{31}$$

This shows that the coupling network in the generalized model consisting of a transformer as well as the coupling elements $G_C$ and $B_C$ is mainly realized by the mutual coupling of the antenna array in [12]. Therefore, this model is a special case of the generalized model presented in this paper with specific demands on the antenna itself. Using the mutual antenna coupling is a viable way to realize the transformer. The influence of the mutual antenna coupling is illustrated by means of the vector plot in Fig. 9. The signal received at one antenna is coupled over to the other antenna and gets scaled and shifted in phase. The output of the coupled antenna array exhibits a higher phase progression than it is supposed to have according to the physical element separation. It can be clearly recognized that a phase gain is obtained solely from the mutual coupled antenna array.

Anyhow, this leads to some limitations when using this model of the biomimetic antenna array. When assuming $\bar{\xi}$=0 (cf. (43)) and inserting the result in the equation for $\bar{\eta}$ (cf. (42)) to eliminate $\bar{b}$ (analogue to Section IV, (21)–(23)) the following relation remains:

$$\bar{\eta} = \frac{(\bar{G}^2 - \bar{G}_{12}^2) + \bar{a}^2\frac{\bar{G}+\bar{G}_{12}}{\bar{G}-\bar{G}_{12}}}{(\bar{G}-\bar{G}_{12})^2 + \bar{a}^2}\,, \tag{32}$$
$$= \frac{\bar{G}+\bar{G}_{12}}{\bar{G}-\bar{G}_{12}} = \frac{\bar{G}_L+\bar{G}_{11}+\bar{G}_{12}}{\bar{G}_L+\bar{G}_{11}-\bar{G}_{12}}\,. \tag{33}$$

This means that for the case $\bar{\xi}$=0 (maximal sensitivity in boresight direction) a phase gain can only be reached if the antenna array has a significant mutual coupling ($\bar{G}_{12}\neq 0$). Otherwise (33) will be in the range of 1 and therefore, no significant phase gain can be reached (cf. [15]).

TABLE I
Y-PARAMETERS OF THE PATCH ANTENNA ARRAY AT 76.5 GHZ OBTAINED FROM FULL WAVE SIMULATIONS.

| | | | |
|---|---|---|---|
| $G_{11}$ | 19.44 mS | $G_{12}$ | 0.009 mS |
| $B_{11}$ | 1.40 mS | $B_{12}$ | 4.62 mS |

For a given antenna with parameters $\bar{G}_{11}$ and $\bar{G}_{12}\neq 0$, there is no maximum for (33) with respect to $\bar{G}_L$. But the right side of (33) is monotonically decreasing with increasing $\bar{G}_L$, i. e., the phase gain is getting smaller with decreasing load resistance $\bar{R}_L$. The maximal theoretical phase gain will be reached for a value of $\bar{G}_L$=0 (open) and calculates to

$$\bar{\eta}_{\text{max}} = \frac{\bar{G}_{11}+\bar{G}_{12}}{\bar{G}_{11}-\bar{G}_{12}}\,. \tag{34}$$

This means the maximum achievable phase gain depends only on the used antenna and cannot be further increased with the coupling network, not even by sacrificing more $L_{\text{out}}$. This can be seen in Fig. 9 where the magnitude of the coupling directly influences the realized phase gain. As a consequence, for antennas with low mutual coupling ($\bar{G}_{12} \ll \bar{G}_{11}$) the achievable phase gain will be very low.

In contrast to that, with the generalized model, an arbitrary phase gain can be achieved for any given antenna by increasing $G_C$ (cf. (23)).

The proposed model describes the biomimetic coupling in its general form. Hence, not only strongly coupled antenna arrays can be used as base antennas. The practical realization of the biomimetic coupling can be done via the mutual antenna coupling ([11], [12]) or with a discrete transformer (this work). Even a combination of both coupling methods can be used.

## VI. Fabrication and Measurement

The generalized model presented in the previous sections was verified by designing and measuring a prototype. To demonstrate that the new model achieves a phase gain even if the antenna array itself is not strongly coupled, an array with a relatively large element separation of $d$=$\lambda/2$ will be used in contrast to, e. g., [12]. An aperture coupled patch antenna with a length of 1 mm (non-radiating edge) and a width of 0.7 mm (radiating edge) is chosen as radiating element for the desired frequency band around 77 GHz. The fabricated antenna array with an element separation of $d$=1.95 mm is depicted in Fig. 10. Both layers of the antenna consist of RO3003 with a thickness of 127 µm each. The antenna Y-Parameters are obtained from full wave simulations and are given in Tab. I.

The biomimetic antenna array shall be designed for a phase enhancement factor of $\eta$=3. Using (25) and (27), the necessary coupling network values can be calculated to $G_C$=78.8 mS and $B_C$=−15.7 mS considering a $G_L$ of 20 mS. This can be realized at 76.5 GHz by a resistor with $R_C$=13 Ω and an inductor with $L_C$=133 pH. Additionally, a transformer for the coupling network has to be designed. An interleaved single layer approach with one and a half turn according to the inset in Fig. 10 was chosen where the wires are 150 µm in width and spaced 100 µm apart. Since the transformer introduces losses

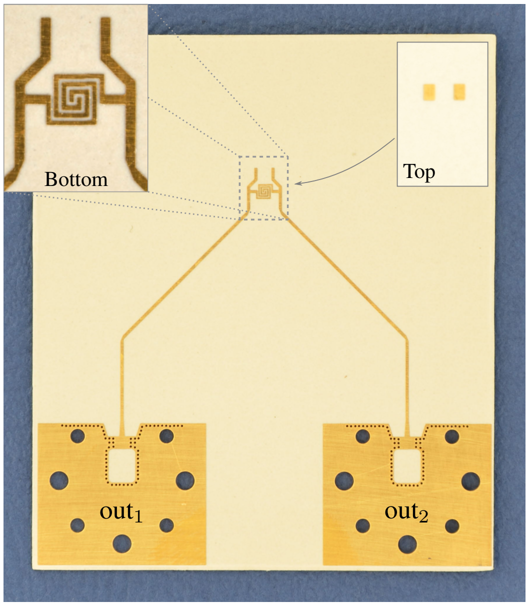


Fig. 10. Layout of the fabricated BMAA using aperture coupled patch antennas (bottom view). The patch antennas are on the top layer (see inset on the top right), the feeding lines and the transformer are on the bottom layer.

and non-ideal phase shifts it is convenient to use these non-idealities to model $G_C$ and $B_C$ by the transmission factor and phase of the transformer. This can be achieved by the following relation which gives the transmission s-parameter for the whole coupling network:

$$s_{21,\text{trafo}} = -\frac{G_C + \mathrm{j}B_C}{Y_0 + G_C + \mathrm{j}B_C} \; . \tag{35}$$

Using (35) with the previously calculated element values results in the following requirements for the transformer:

$$|s_{21}| = -1.9\,\text{dB} \qquad \arg\left(s_{21}\right) = 177.8^\circ \; . \tag{36}$$

The transformer was optimized by using full wave simulations to match the calculated requirements as close as possible. The outer dimensions of the used transformer are $(1.7 \times 1.9)\,\text{mm}^2$.

The fabricated antenna with and without coupling network was measured in an anechoic chamber using a robot [27]. With a horn antenna mounted on the robotic arm the H-plane of the antenna under test (AUT) was sampled at a constant distance. The transmission factor between the AUT and the horn antenna was measured for both ports using a vector network analyzer with external frequency converters for the E-band. To ensure comparability, the measurement setup was identical for both AUTs.

Fig. 11(a) shows the measured output phase difference and Fig. 11(b) the measured normalized output power level at $76.5\,$GHz. A phase gain of approximately $\eta{=}2$ has been achieved at a normalized output power level of around $L_{\text{out}}{=}{-}4\,$dB. The measured phase gain is less than the simulated value. A possible reason for this might be higher dielectric losses of the PCB compared to the assumptions made in the simulation model, and therefore, a lower transmission factor of the transformer leads to a lower phase gain. Consequently, the measured normalized output power level $L_{\text{out}}$ is higher compared to the simulated value.

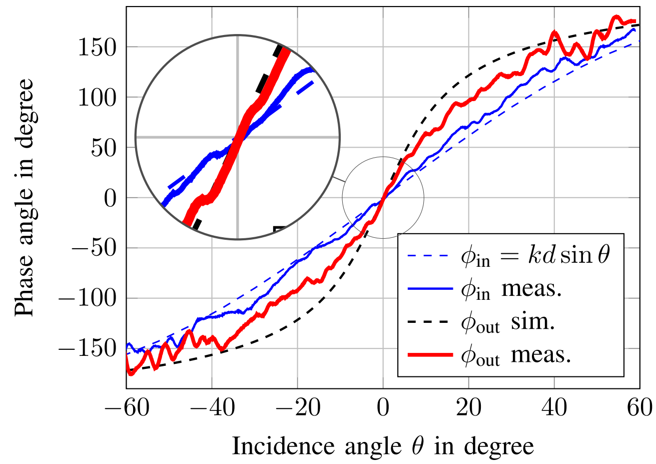


(a)

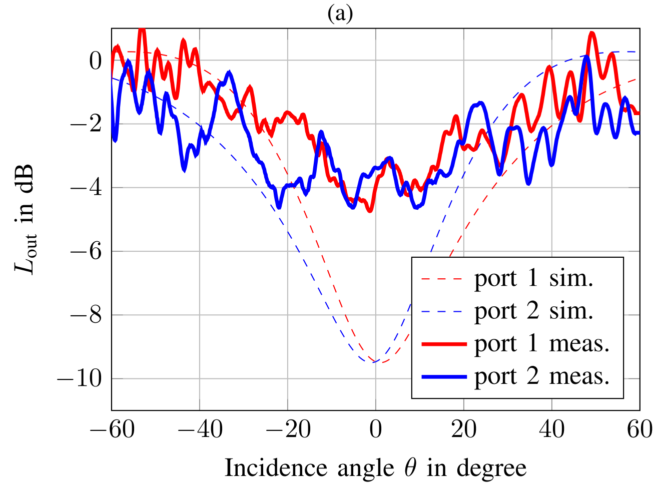


(b)

Fig. 11. Simulated and measured phase difference curves (a) and output power levels $L_{\text{out}}$ (b) for the fabricated biomimetic antenna array at $76.5\,$GHz.

The measurements show that the generalized model presented in this work and the corresponding design process are working as expected. A phase gain compared to a conventional antenna can be clearly recognized leading to an improved angle estimation capability of the presented BMAA. According to the electrical model of [12], the antenna used in this work would have only showed a phase gain of less than 1.001 (cf. (34)) due to the low mutual antenna coupling.

## VII. Conclusion

In this paper, a generalized electrical model of the biomimetic antenna array has been introduced. Apart from an intuitive understanding of the working principle of the biomimetic antenna array, the generalized model allows the use of basically every antenna element in a BMAA. The strong mutual coupling which was mandatory before is not needed anymore. After showing the working principle, a design process for a desired phase enhancement factor $\eta$ was given and a prototype was successfully designed, fabricated, and measured.

## APPENDIX
## EQUATIONS FROM PREVIOUS WORKS

A number of equations of [12] are necessary for the derivations in this paper. However, some of these formulas are not given or were not fully derived in [12]. For better understanding, especially when comparing the different models in Section V, these formulas are given in the following:

$$\bar{G} = \bar{G}_L + \bar{G}_{11} \tag{37}$$

$$\bar{a} = \bar{B}_{11} - \bar{B}_{12} + \bar{B}_1 + \bar{B}_2 \tag{38}$$

$$\bar{b} = \bar{B}_{11} + \bar{B}_{12} + \bar{B}_1 \tag{39}$$

$$\frac{\bar{u_2}}{\bar{u_1}} = \frac{1 + \mathrm{j}\bar{z}\tan\alpha}{1 - \mathrm{j}\bar{z}\tan\alpha} \approx \frac{1 + \mathrm{j}\bar{z}\alpha}{1 - \mathrm{j}\bar{z}\alpha} \tag{40}$$

$$\bar{z} = \frac{\bar{G} + \bar{G}_{12} + \mathrm{j}\bar{b}}{\bar{G} - \bar{G}_{12} + \mathrm{j}\bar{a}} \tag{41}$$

$$\bar{\eta} = \mathrm{Re}(\bar{z}) = \frac{(\bar{G}^2 - \bar{G}_{12}^2) + \bar{a}\bar{b}}{(\bar{G} - \bar{G}_{12})^2 + \bar{a}^2} \tag{42}$$

$$\bar{\xi} = \mathrm{Im}(\bar{z}) = \frac{\bar{G}(\bar{b} - \bar{a}) - \bar{G}_{12}(\bar{b} + \bar{a})}{(\bar{G} - \bar{G}_{12})^2 + \bar{a}^2} \tag{43}$$

## ACKNOWLEDGMENT

The authors would like to thank Dr.-Ing. Michael Buchholz of the Institute of Measurement, Control and Microtechnology at Ulm University for the valuable discussions.
This work was funded by the German Research Foundation (DFG, Deutsche Forschungsgemeinschaft) – WA 3506/6-1.

## REFERENCES

[1] X. Yu and H. Xin, "Direction-of-Arrival Estimation Enhancement for Closely Spaced Electrically Small Antenna Array," *IEEE Trans. Microw. Theory Techn.*, vol. 66, no. 1, pp. 477–484, Jan. 2018.

[2] M. J. Slater, C. D. Schmitz, M. D. Anderson, D. L. Jones, and J. T. Bernhard, "Demonstration of an Electrically Small Antenna Array for UHF Direction-of-Arrival Estimation," *IEEE Trans. Antennas Propag.*, vol. 61, no. 3, pp. 1371–1377, Mar. 2013.

[3] S. Hwang, S. Burintramart, T. K. Sarkar, and S. R. Best, "Direction of Arrival (DOA) Estimation Using Electrically Small Tuned Dipole Antennas," *IEEE Trans. Antennas Propag.*, vol. 54, no. 11, pp. 3292–3301, Nov. 2006.

[4] A. C. Mason, M. L. Oshinsky, and R. R. Hoy, "Hyperacute directional hearing in a microscale auditory system," *Nature*, vol. 410, no. 6829, pp. 686–690, Apr. 2001. [Online]. Available: http://www.nature.com/nature/journal/v410/n6829/full/410686a0.html

[5] R. N. Miles, D. Robert, and R. R. Hoy, "Mechanically coupled ears for directional hearing in the parasitoid fly Ormia ochracea," *J. Acoust. Soc. Am.*, vol. 98, no. 6, pp. 3059–3070, Dec. 1995.

[6] R. N. Miles, Q. Su, W. Cui, M. Shetye, F. L. Degertekin, B. Bicen, C. Garcia, S. Jones, and N. Hall, "A low-noise differential microphone inspired by the ears of the parasitoid fly Ormia ochracea," *J. Acoust. Soc. Am.*, vol. 125, no. 4, pp. 2013–2026, Apr. 2009. [Online]. Available: https://www.ncbi.nlm.nih.gov/pmc/articles/PMC2677264/

[7] A. Ishfaque and B. Kim, "Fly Ormia Ochracea Inspired MEMS Directional Microphone: A Review," *IEEE Sensors J.*, vol. 18, no. 5, pp. 1778–1789, Mar. 2018.

[8] N. Behdad, M. A. Al-Joumayly, and M. Li, "Biomimetic electrically small antennas," *Electron. Lett.*, vol. 46, no. 25, pp. 1650–1651, Dec. 2010.

[9] N. Behdad, M. A. Al-Joumayly, and M. Li, "Biologically Inspired Electrically Small Antenna Arrays With Enhanced Directional Sensitivity," *IEEE Antennas Wireless Propag. Lett.*, vol. 10, pp. 361–364, Apr. 2011.

[10] N. Behdad, A. R. Masoumi, and Y. Yusuf, "On the Design and Optimization of Biomimetic Electrically Small Antenna Arrays," in *Proc. IEEE Int. Workshop on Antenna Tech. (iWAT)*, Mar. 2012, pp. 347–350.

[11] A. R. Masoumi, Y. Yusuf, and N. Behdad, "Biomimetic Antenna Arrays Based on the Directional Hearing Mechanism of the Parasitoid Fly Ormia Ochracea," *IEEE Trans. Antennas Propag.*, vol. 61, no. 5, pp. 2500–2510, May 2013.

[12] A. R. Masoumi and N. Behdad, "An Improved Architecture for Two-Element Biomimetic Antenna Arrays," *IEEE Trans. Antennas Propag.*, vol. 61, no. 12, pp. 6224–6228, Dec. 2013.

[13] G. Fontgalland, Z. Wang, and J. L. Volakis, "Small Biomimetic Array for Direction Finding and Superdirectivity," in *Proc. URSI Int. Symp. on Electromagnetic Theory (EMTS)*, May 2013, pp. 88–89.

[14] J. Zhong, A. Kiourti, and J. L. Volakis, "Reducing and Controlling the Beamwidth of Electrically Small Antenna Arrays," in *Proc. 9th Eur. Conf. on Antennas and Propag. (EuCAP)*, Apr. 2015, pp. 1–2.

[15] P. Grüner, T. Chaloun, and C. Waldschmidt, "Towards a mm-Wave Planar Biomimetic Antenna Array with Enhanced Phase Sensitivity," in *Proc. 10th Eur. Conf. on Antennas and Propag. (EuCAP)*, Davos, Apr. 2016, pp. 1–5.

[16] A. R. Masoumi and N. Behdad, "Architecture, Design, and Nonlinear Optimization of Three-Element Biomimetic Antenna Arrays," *IEEE Antennas Wireless Propag. Lett.*, vol. 12, pp. 1416–1419, Nov. 2013.

[17] M. R. Nikkhah, K. Ghaemi, and N. Behdad, "A Three-Element Biomimetic Antenna Array With an Electrically Small Triangular Lattice," *IEEE Trans. Antennas Propag.*, vol. 65, no. 8, pp. 4007–4016, Aug. 2017.

[18] F. T. Dagefu, J. Oh, and K. Sarabandi, "A Sub-Wavelength RF Source Tracking System for GPS-Denied Environments," *IEEE Trans. Antennas Propag.*, vol. 61, no. 4, pp. 2252–2262, Apr. 2013.

[19] A. M. Elfrgani and R. G. Rojas, "Biomimetic Antenna Array Using Non-Foster Network to Enhance Directional Sensitivity Over Broad Frequency Band," *IEEE Trans. Antennas Propag.*, vol. 64, no. 10, pp. 4297–4305, Oct. 2016.

[20] M. R. Nikkhah, K. Ghaemi, and N. Behdad, "An Electronically Tunable Biomimetic Antenna Array," *IEEE Trans. Antennas Propag.*, vol. 66, no. 3, pp. 1248–1257, Mar. 2018.

[21] M. Akcakaya and A. Nehorai, "Biologically Inspired Coupled Beampattern Design," in *Proc. Int. Waveform Diversity and Design Conf. (WDD)*, Niagara Falls, ON, Canada, Aug. 2010, pp. 48–52.

[22] M. Akcakaya and A. Nehorai, "Performance analysis of the Ormia ochracea's coupled ears," *J. Acoust. Soc. Am.*, vol. 124, no. 4, pp. 2100–2105, Oct. 2008.

[23] M. Akcakaya, C. H. Muravchik, and A. Nehorai, "Biologically Inspired Coupled Antenna Array for Direction of Arrival Estimation," in *Proc. 44th Asilomar Conf. on Signals, Systems and Computers (ASILOMAR)*, Nov. 2010, pp. 1961–1965.

[24] P. Grüner, T. Chaloun, and C. Waldschmidt, "Enhanced Angle Estimation Accuracy of Ultra Compact Radars Inspired by a Biomimetic Approach," in *Proc. IEEE MTT-S Int. Microwave Symp. (IMS)*, Honolulu, HI, Jun. 2017.

[25] A. R. Masoumi, K. Ghaemi, and N. Behdad, "A Two-Element Biomimetic Antenna Array With Enhanced Angular Resolution and Optimized Power Extraction," *IEEE Trans. Antennas Propag.*, vol. 63, no. 3, pp. 1059–1066, Mar. 2015.

[26] P. Grüner, S. Nguyen, T. Chaloun, and C. Waldschmidt, "Enhancing Angle Estimation for Off-Boresight Targets Using Biomimetic Antenna Arrays," in *Proc. 48th Eur. Microwave Conf. (EuMC)*, Madrid, Sep. 2018.

[27] L. Boehm, S. Pledl, F. Boegelsack, M. Hitzler, and C. Waldschmidt, "Robotically Controlled Directivity and Gain Measurements of Integrated Antennas at 280 GHz," in *Proc. 45th Eur. Microwave Conf. (EuMC)*. IEEE, Sep. 2015.

**Patrik Grüner** (S'15) received the M.Sc. degree in electrical engineering from Ulm University, Ulm, Germany, in 2015, where he is currently pursuing the Ph.D. degree. In 2015, he joined the Institute of Microwave Engineering (MWT), Ulm University. His current research interests include compact FMCW radar sensors and biomimetic antenna systems both in the microwave and millimeter-wave range.

Mr. Grüner was a recipient of the ARGUS Science Award in 2013 and the Best Paper Award of the 2013 International Workshop on Antenna Technology.

**Tobias Chaloun** (S'10-M'16) received the Dipl.-Ing. degree and the Dr.-Ing. degree (with honors) in electrical engineering both from the University of Ulm, Ulm, Germany, in 2010 and 2016, respectively.

From 2010 to 2016, he was a Research Assistant at the Institute of Microwave Engineering (MWT), Ulm University, Germany where he conducted his doctoral studies in the field of highly-integrated antenna systems for communication applications at millimeter wave frequencies.

Since January 2017, he is a Senior Researcher and Lecturer at the Institute of Microwave Engineering. His main research interest concerns multilayer antennas and circuits, millimeter-wave packaging and interconnects, phased array antenna systems and millimeter-wave radar sensors.

Dr. Chaloun is member of the European Microwave Association and the Institute of Electrical and Electronics Engineers. Currently, he serves as a reviewer for the IEEE TRANSACTIONS ON ANTENNAS AND PROPAGATION and IEEE TRANSACTIONS ON MICROWAVE THEORY AND TECHNIQUES.

Dr. Chaloun was the recipient of the Best Paper Award at the German Microwave Conference in 2015. In 2016, he has been awarded for the Best Paper in the IET Microwaves, Antennas & Propagation.

**Christian Waldschmidt** (S'01-M'05-SM'13) received the Dipl.-Ing. (M.S.E.E.) and the Dr.-Ing. (Ph.D.E.E.) degrees from the University Karlsruhe (TH), Karlsruhe, Germany, in 2001 and 2004, respectively. From 2001 to 2004 he was a Research Assistant at the Institut für Höchstfrequenztechnik and Elektronik (IHE), Universität Karlsruhe (TH), Germany. Since 2004 he has been with Robert Bosch GmbH, in the business units Corporate Research and Chassis Systems. He was heading different research and development teams in microwave engineering, rf-sensing, and automotive radar.

In 2013 Christian Waldschmidt returned to academia. He was appointed as the Director of the Institute of Microwave Engineering at University Ulm, Germany, as full professor. The research topics focus on radar and rf-sensing, mm-wave and submillimeter-wave engineering, antennas and antenna arrays, rf and array signal processing. He authored or coauthored over 120 scientific publications and more than 20 patents. Additionally, he is chair of IEEE MTT-27 Technical Committee (wireless enabled automotive and vehicular applications), executive committee board member of the German MTT/AP joint chapter, and member of the ITG committee Microwave Engineering (VDE). In 2015 and 2018 he served as the TPC chair and in 2017 as TPC-Co-Chair of the IEEE MTT International Conference on Microwaves for Intelligent Mobility. He is a reviewer for multiple IEEE transactions and several conferences like IMS and EUMW.